Room temperature NO_2-sensing properties of hexagonal tungsten oxide nanorods*

Yaqiao Wu(武雅乔)[1,2], Ming Hu(胡明)[1,†], and Yuming Tian(田玉明)[2]

[1] School of Electronics and Information Engineering, Tianjin University, Tianjin 300072, China
[2] Taiyuan University of Science and Technology, Taiyuan 030024, China

(Received 30 August 2016; revised manuscript received 21 October 2016; published online 20 December 2016)

Hexagonal WO_3 nanorods were synthesized through a facile hydrothermal method. The nanorods properties were investigated by scanning electron microscope (SEM), transmission electron microscope (TEM), energy dispersive spectroscopy (EDS), and x-ray diffraction (XRD). The NO_2-sensing performances in terms of sensor response, response/recovery times and repeatability at room temperature were optimized by varying the heat treatment temperature of WO_3 nanorods. The optimized NO_2 sensor (400-°C-annealed WO_3 nanorods) showed an ultra-high sensor response of 3.2 and short response time of 1 s to 5-ppm NO_2. In addition, the 400-°C-annealed sample exhibited more stable repeatability. Furthermore, dynamic responses measurements of annealed samples showed that all the annealed WO_3 nanorods sensors presented p-type behaviors. We suppose the p-type behavior of the WO_3 nanorods sensor to be that an inversion layer is formed in the space charge layer when the sensor is exposed to NO_2 at room temperature.Therefore, the 400-°C-annealed WO_3 nanorods sensor is one of the most energy conservation candidates to detect NO_2 at room temperature.

Keywords: WO_3 nanorods, thermal treatment, NO_2 gas sensor, room temperature

PACS: 07.07.Df, 78.67.Qa, 61.46.Df **DOI:** 10.1088/1674-1056/26/2/020701

1. Introduction

According to the EPA (United States Environmental Protection Agency), NO_2 is used as the indicator for the larger group of nitrogen oxides. NO_2 is the main source in the production of ground-level ozone and fine particle pollution except for contributing to the formation of acid rain and smog. Therefore, in January 2010, EPA established an additional primary standard for NO_2 at 100 ppb, averaged over one hour. In order to detect NO_2, many researchers have reported nanostructure metal oxide based NO_2 sensors.[1–8] These gas sensors usually were operated at the temperature range of 100 °C–300 °C resulting in high electrical power consumption, which limited the use of the metal oxide based sensor as a sensing element in battery-powered portable devices.[9] Among various nanostructure metal oxide semiconductor materials, tungsten oxide nanorods/nanowires, which can achieve a low operation temperature since WO_3 has a lower integrating energy barrier than SnO_2 or TiO_2,[10–16] are highly promising candidates for detecting NO_2. Therefore, it is prospective to develop a low-cost, low power consumption, high-sensitivity and stable NO_2 gas sensor based on tungsten oxide nanorods/nanowires.

In most cases, sensing films were prepared by wet chemical methods, so the process of thermal treatment is a necessary step, which not only can burn out the organic solvent used in preparation of coating slurry but also can enhance the adherence between the sensing film and the sensor substrates. More importantly, thermal treatment could stabilize the sensing film's microstructure and then improve the reliability and stability of the gas sensor.[17] However, the gas sensing material would gradually undergo a series of morphological evolutions and obvious changes of phase composition with the increase of temperature. On the other hand, these changes are the main factors which would influence the gas-sensing properties of oxide semiconductor based sensors.[18] Therefore, it is significant to comprehensively understand the relationship between the annealing-induced microstructure changes and the gas-sensing properties of the one-dimensional tungsten oxide.

Next, metal oxides based gas sensors are classified as n-type or p-type according to whether they show a decrease or an increase of conductivity when they are exposed to an oxidizing gas (such as NO_2).[19,20] WO_3 nanorods sensors which were operated at high temperature are known to behave as an n-type semiconductor.[21–25] The p-type semiconductor based on WO_3 nanorods operating at room temperature is rarely reported. Consequently, this paper is focused on the sensing property of WO_3 nanorods sensor at room temperature.

In this study, WO_3 nanorods are prepared by a facile hydrothermal method and the relationship is investigated between the microstructures and gas sensing properties of WO_3 nanorods sensors annealed at 300, 400, and 500 °C, respectively. In addition, the p-type semiconductor gas sensing

*Project supported by the National Natural Science Foundation of China (Grant Nos. 60771019, 61271070, and 61274074) and the Tianjin Key Research Program of Application Foundation and Advanced Technology, China (Grant No. 11JCZDJC15300).

†Corresponding author. E-mail: huming@tju.edu.cn

© 2017 Chinese Physical Society and IOP Publishing Ltd

mechanism of the WO_3 nanorods sensor is discussed.

2. Experimental section

2.1. Synthesis of WO_3 nanorods

WO_3 nanorods were synthesized through hydrothermal technology. In a typical procedure, 0.01-mol $Na_2WO_4{\cdot}2H_2O$ and 0.02-mol NaCl were dissolved in 60-ml deionized water and stirred for 30 min by magnetic stirring apparatus. $Na_2WO_4{\cdot}2H_2O$ was served as a precursor and NaCl was used as structure directing agents (SDAs) which have been proven to facilitate the controllable growth of nanostructure WO_3. The pH value of the solution was fixed at 2.5 which was adjusted by using 3-M HCl solution. Then, the obtained uniform mixture was transferred into a 100-ml Teflon-lined stainless steel autoclave and heated at 180 °C for 24 h in an electric oven. After naturally cooling down to room temperature, the resultant precipitates were washed with deionized water and ethanol by a centrifuger several times and dried in a vacuum at 80 °C for 10 h. Finally, the slurry of as-prepared tungsten oxide nanorods was prepared by ultrasonically mixing tungsten oxide nanorods and terpineol, which acted as a vehicle binder and solvent. In this experiment, all reagents were purchased from the Guangfu Fine Chemical Research Institute (Tianjin, China).

2.2. Sensor fabrication and NO_2 response measurement

Firstly, a pair of interdigital Pt electrodes was deposited on the cleaned alumina substrates by RF magnetron sputtering using a shadow mask. In detail, the DPS–III ultrahigh vacuum facing-target magnetron sputtering system was used to deposit Pt electrical contacts and operating parameters were listed as follows: the RF power was 90 W, the base vacuum pressure was 4.0×10^{-4} Pa and the working pressure was 2 Pa. Secondly, the coating slurry was prepared by mixing the nanorods (30 mg) in terpineol (0.2 ml) and then ground in an agate mortar for 30 min to obtain a homogeneous paste. The resulting paste was coated on those alumina substrates by the spin-coating method. Thirdly, the WO_3 nanorods sensors were annealed at 300, 400, and 500 °C for 2 h in the air with a heating rate of 6 °C/min, respectively. Then the gas-sensing characteristics of as-prepared sensors were tested in a computer-controlled static gas sensing characterization system which consists of a 30-L sealed organic glass test chamber, a professional digital multi-meter, a data acquisition system and a flat heating plate with an adjustment range from room temperature (RT) to 300 °C.[26] The programmable multi-meter was connected to the data acquisition system, which was used for continuously recording the resistance changes of the sensor and the sampling interval was set to 1 s. The schematic diagram of the sensor and the measurement system are depicted in Fig. 1. When exposed to NO_2, the sensor response presented a p-type feature at room temperature. Hence, the response is defined as $S = R_a/R_g$, where R_a and R_g are the resistances of the sensor element in the presence of atmospheric air and target gas respectively. The time taken by the sensor to achieve 90% of the total resistance change is defined as the response and recovery time.

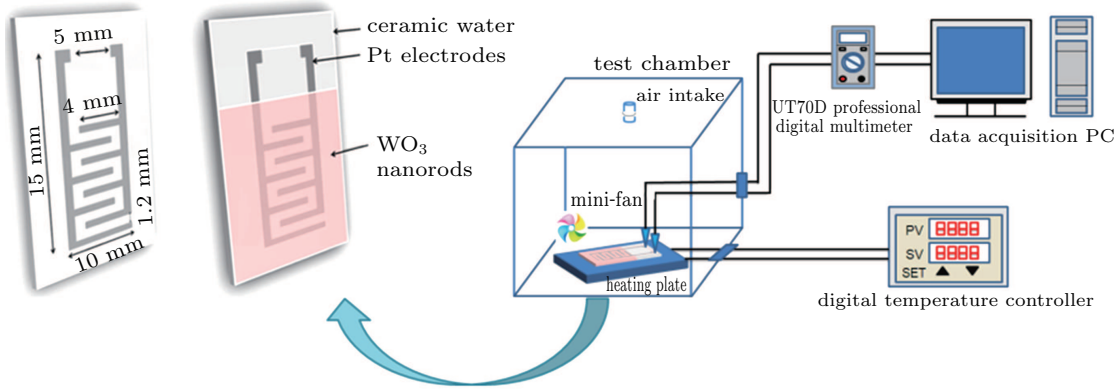


Fig. 1. (color online) The schematic diagram of the sensor and the measurement system.

2.3. Characterization of WO_3 nanorods

The morphology, element composition and crystal structure of the WO_3 nanorods were characterized using a field emission scanning electron microscope (FE-SEM, FEI Nanosem 430), energy dispersive spectroscopy (EDS) attached on the FESEM, transmission electron microscope (TEM, TECNAIG2F-20) and x-ray diffraction (XRD, RIGAKU D/MAX 2500V/PC, Cu Kα radiation).

3. Results and discussion

3.1. Effects of annealing on microstructure

Typical FESEM image of as-synthesized WO_3 nanorods is shown in Fig. 2(a), from which we can see that those nanorods exhibit a one dimension structure with lengths in the range of 3 μm–5 μm and cross sections in the range of 50 nm–150 nm. Nevertheless, there still exist nanorod bundles which are induced by larger surface areas and their intrin-

sic defects such as shear planes, oxygen vacancies, and stacking faults.[27,28] Further characterizations of the morphology and crystallinity of the WO_3 nanorods were investigated by TEM and high resolution transmission electron microscope (HRTEM) as shown in Fig. 2(b) and Fig. 2(c). It can be seen that the lattice fringe separation is about 0.323 nm, corresponding to the lattice space of the hexagonal WO_3 (200) plane. In order to investigate the morphology evolution of WO_3 nanorods with increasing annealing temperature, the SEM images of annealed WO_3 nanorods coated on ceramic wafer by spin coating are illustrated in Fig. 3. The appearance of annealed nanorods is changed pronouncedly compared with that of raw WO_3 nanorods (Fig. 2(a)). After being processed at 300 °C for 2 h, the diameter of all the nanorods is still in the range of 50 nm–150 nm but the lengths reduce sharply through a fracture of nanorods (Fig. 3(a)). The morphology feature remains stable after annealing at 400 °C (Fig. 3(b)). When increasing the temperature to 500 °C, it is apparent that the morphological characteristic of the nanorods almost disappears completely, and nanoparticles which display pronounced facet structures with polygonal cross-sections are formed instead, indicating that a possible agglomeration occurs (Fig. 3(c)).

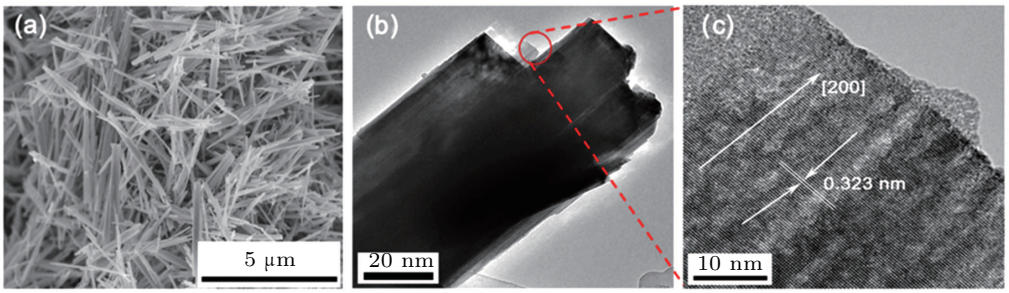


Fig. 2. (color online) SEM, TEM, and HRTEM images of WO_3 nanorods.

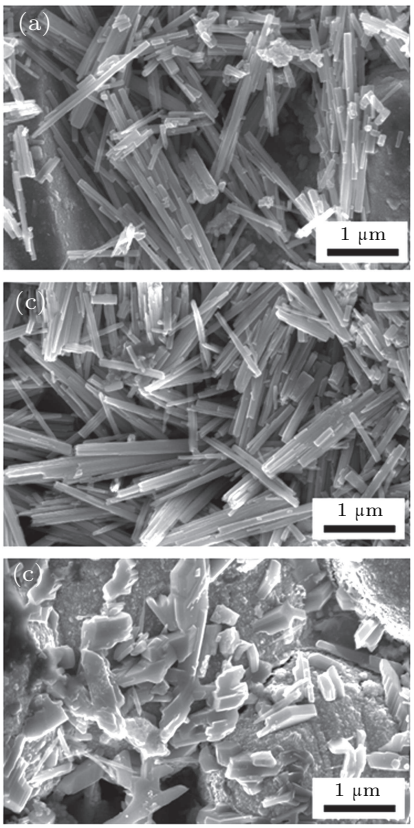


Fig. 3. SEM images of WO_3 nanorods after (a) 300-°C, (b) 400-°C, and (c) 500-°C thermal treatment.

The surface morphology of the square-marked area and the corresponding EDS spectrum of WO_3 nanorods with annealed samples are shown in Fig. 4. Every EDS spectrum contains the characteristic peaks of C, O, Na, and W, and all the annealed sensors still include the characteristic peaks of Al and Pt. The elements concentration of (a) the pristine WO_3 nanorods together with (b) 300-°C-annealed, (c) 400-°C-annealed, and (d) 500-°C-annealed sensor are illustrated in Table 1.

Table 1. The elements concentration of (a) the pristine WO_3 nanorods together with (b) 300-°C-annealed, (c) 400-°C-annealed, and (d) 500-°C-annealed sensor.

	(a)	(b)	(c)	(d)
Element	Weight%	Weight%	Weight%	Weight%
C	0.7	0.67	0.56	0.78
O	26.85	24.69	22.82	23.99
Na	2.05	1.55	1.76	2.37
Al	0	1.88	3.68	0
W	70.39	54.14	54.70	41.49
Pt	0	17.08	16.47	31.38
Totals	100	100	100	100

The elements concentration of (a) the pristine WO_3 nanorods together with (b) 300-°C-annealed, (c) 400-°C-annealed, and (d) 500-°C-annealed sensor are illustrated in Table 1. The sum of the weight concentrations is equal to 100%.The atomic ratio of W and O should be 1:3 as a result of the chemical reaction, but their measuring value of atomic ratio calculated by EDS quantitative analysis software is (a) 1:4, (b) 1:5, (c) 1:5, and (d) 1:7. We surmised the additional O atomic of the pristine WO_3 nanorods and 500-°C-annealed samples may come from adsorbed oxygen and NaO which is the residual decomposition product of $Na_2WO_4{\cdot}2H_2O$. Besides the above three O elements supplies, a portion of O elements come from Al_2O_3 substrate owing to that we have de-

tected an Al element in the 300-°C- and 400-°C-annealed samples. The Pt elements in the EDS may come from the alumina substrates deposited with a pair of interdigital Pt electrodes. This can be certified by the result of XRD analysis. The appearance of the C element can be attributed to the SEM grid.

In order to estimate O elements weight% derived from adsorbed oxygen, we have calculated the O elements weight% derived from other oxide. For example, the relative molar mass of W and O in the WO_3 molecule is 184:48. The weight% of W elements is 70.39% in the pristine WO_3 nanorods, so the weight% of O elements in WO_3 is 18.36%.The results are shown in Table 2.

Table 2. The weight% of O elements of (a) the pristine WO_3 nanorods together with (b) 300-°C-annealed, (c) 400-°C-annealed, and (d) 500-°C-annealed sensor.

	(a)	(b)	(c)	(d)
Total O elements weight%	26.85	24.69	22.82	23.99
O elements derived from WO_3	18.36	14.12	14.30	10.82
O elements derived from Al_2O_3	–	1.67	3.27	–
O elements derived from Na_2O	0.71	0.54	0.61	0.82
O elements derived from adsorbed oxygen	7.78	8.36	4.64	12.35

On the basis of Table 2, we further estimated the weight% of adsorbed oxygen/μm^2 of (a) the pristine WO_3 nanorods together with (b) 300-°C-annealed, (c) 400-°C-annealed, and (d) 500-°C-annealed sensor. The results are shown in Table 3. The weight% of adsorbed oxygen/μm^2 increased by the way of heat treatment. Considering the sample room of EDS or SEM is pumped into a vacuum state before scanning, the adsorbing power between oxygen and WO_3 nanorods should be a chemical bond instead of a physical bond. The chemical bond contains an electrovalent bond and a covalent bond, which were produced by lots of oxygen vacancies. Thus, we consider the oxygen vacancies increased in the nanorods by the way of heat treatment, which can be further confirmed by the XRD.

Table 3. The weight% of adsorbed oxygen/μm^2 of (a) the pristine WO_3 nanorods together with (b) 300-°C-annealed, (c) 400-°C-annealed, and (d) 500-°C-annealed sensor.

	(a)	(b)	(c)	(d)
O elements derived from adsorbed oxygen	7.78	8.36	4.64	12.35
Scanning area of the square-marked area (μm^2)	295.50	55.25	14.40	1.44
Weight% of adsorbed oxygen/μm^2	0.03	0.15	0.32	8.57

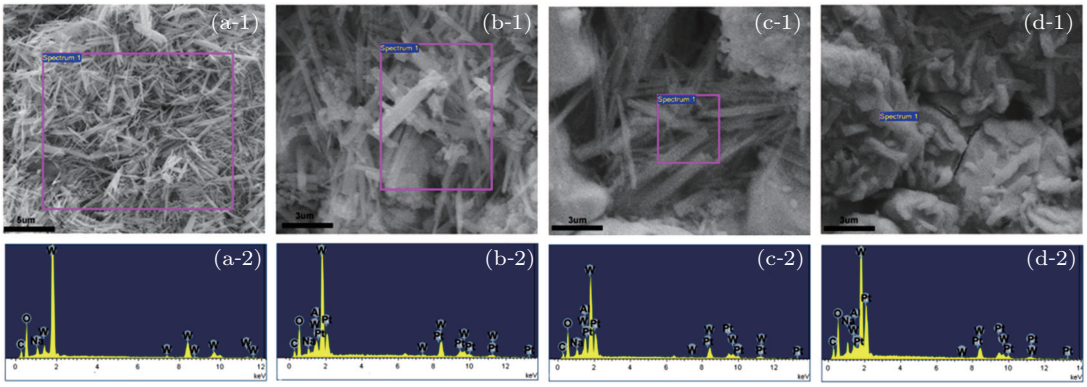


Fig. 4. (color online) The surface morphology of selected area and corresponding EDS spectrum of (a) WO_3 nanorods, (b) 300-°C-, (c) 400-°C-, and (d) 500-°C-annealed samples.

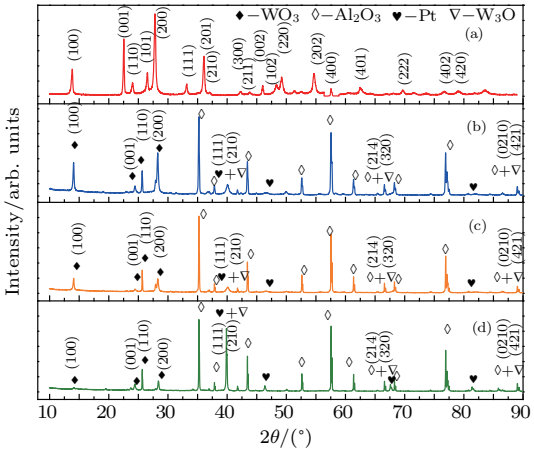


Fig. 5. (color online) XRD patterns of (a) freshly-obtained WO_3 nanorods, (b) 300-°C-, (c) 400-°C-, and (d) 500-°C-annealing WO_3 nanorods.

The crystalline phases of WO_3 nanorods annealed at different temperatures together with the pristine WO_3 nanorods were analyzed by x-ray diffraction. The XRD patterns of the original WO_3 nanorods match well with JCPDS NO. 33-1387 for hexagonal WO_3 as indicated in Fig. 5(a). In order to avoid the WO_3 nanorods being polluted, we directly take the prepared sensors as a test specimen for XRD analysis. Therefore, the main crystalline phases of annealed ones are Al_2O_3 (JCPDS NO. 46-1212) and Pt (JCPDS NO. 87-0646) except hexagonal WO_3 (JCPDS NO. 75-2187). However, it is noteworthy that a new crystalline phase of cubic W_3O (JCPDS NO. 02-1138) present in annealed samples as shown in Figs. 5(b), 5(c), 5(d). Its three characteristic peaks which are the (210) peak with $I = 100$ ($2\theta = 40.040$), the (320) peak with $I = 60$ ($2\theta = 66.761$), and the (421) peak with $I = 70$ ($2\theta = 88.895$) match together the Pt (111) peak

with $I = 100$ ($2\theta = 39.796$), the Al_2O_3 (214) peak with $I = 23$ ($2\theta = 66.519$), and the Al_2O_3 (0210) peak with $I = 9$ ($2\theta = 88.994$). W_3O is a kind of metastable and non-stoichiometry tungsten oxide, which has a large number of oxygen vacancies. As the temperature is increased to 500 °C, the characteristic peak of Pt ($2\theta = 67.859$) also appears. This is a result of the high annealing temperature making the Pt electrodes be exposed to the outside.

3.2. Effects of annealing on gas-sensing properties

We have examined the 300-°C annealed sample by sensing 1-ppm NO_2 from room temperature to 250 °C and the sensor showed two completely different sensing behaviors. The WO_3 nanorods sensor showed a p-type response at the range of 25 °C–50 °C while an n-type response at the range of 50 °C–250 °C. This work has been published in Ref. [29]. The p-type semiconductor based on WO_3 nanorods operating at room temperature is rarely reported. Consequently, this paper is focused on the sensing property of WO_3 nanorods sensor at room temperature.

Figure 6 depicts the dynamic responses of the gas sensors based on the WO_3 nanorods annealed at (a) 300 °C, (b) 400 °C, and (c) 500 °C to varying NO_2 concentration at room temperature (RT). Figure 7 illustrates the relationship between (a) the response time, (b) the recovery time and NO_2 concentration for the sensors based on annealed WO_3 nanorods at RT. As shown in Figs. 6(a)–6(c) and Fig. 7(a), the WO_3 nanorods sensors are highly sensitive to NO_2 for the resistance of all the sensors decrease abruptly for the NO_2 injection period (shadow areas) and can approach the steady-state values within 75 s. In particular, the response time of the 400-°C-annealed sample reduce to 1 s when the sample is exposed to NO_2 gas with a concentration of either 3 ppm or 5 ppm. As shown in Figs. 6(a)–6(c) and Fig. 7(b), after the removal of NO_2, the resistance of all the annealed WO_3 nanorods sensors increases and is able to recover to the original value within 200 s. The recovery time reduces to 97 s for 3-ppm NO_2 and 152 s for 5-ppm NO_2, respectively. Figure 6(d) illustrates the response of the sensors based on annealed WO_3 nanorods to varying NO_2 concentration at RT. The variation trend of all annealed WO_3 nanorods sensors is similar in that the response increases apparently with increasing NO_2 concentration. In the case of the 400-°C-annealed sample, there is an obvious increase in the response, with the maximum responses of about 1.3 ppm to 0.5 ppm, 1.7 ppm to 1 ppm, 2.3 ppm to 3 ppm and 3.2 ppm to 5 ppm NO_2, respectively. When the heat treatment temperature is increased to 500 °C, the gas sensing property suddenly gets worse. The maximum response is 1.5, when even exposing to 5 ppm. In addition, there is only a slight enhancement in response with increasing NO_2 concentration. We assume that the deteriorated sensing properties probably are related with the reduced specific surface areas (Fig. 3(c)). Excepting the recovery time of 500-°C-annealed sensor is shorter than 400-°C-annealed sensor to 5 ppm NO_2, in every NO_2 concentration, the response time and the recovery time of the 400-°C-annealed sample (red column) is shorter than the 300-°C-annealed sample (yellow column) and the 500-°C-annealed sample (blue column) as shown in Fig. 8.

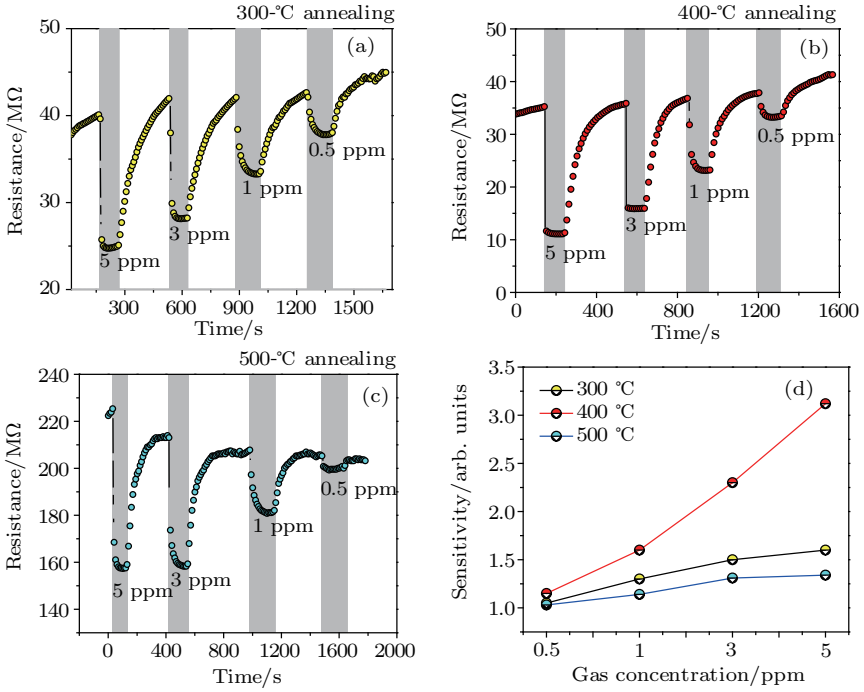


Fig. 6. (color online) Dynamic responses of the gas sensors based on the WO_3 nanorods annealed at (a) 300 °C, (b) 400 °C, and (c) 500 °C to varying NO_2 concentration at room temperature. (d) Relationship between the responses and NO_2 concentration for the sensors based on annealed tungsten WO_3 nanorods at room temperature.

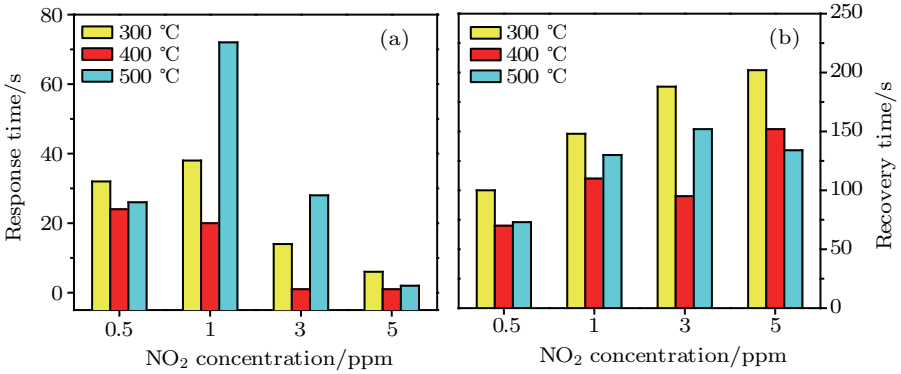


Fig. 7. (color online) Relationship between (a) the response time (b) recovery time and NO_2 concentration for the sensors based on annealed tungsten WO_3 nanorods at room temperature.

In a word, from Fig. 6 and Fig. 7 we can see that the 400-°C-annealed sample has more excellent sensing performance at room temperature compared with both 300-°C- and 500-°C-annealed WO_3 nanorods sensors. We suppose that the excellent gas sensing properties of the 400-°C-annealed sample could be attributed to its moderate crystallinity, larger specific surface areas and more oxygen vacancies. Therefore, the excellent gas sensing properties of hydrothermal-prepared WO_3 nanorods make it an ideal candidate for detecting NO_2 at room temperature.

3.3. Gas-sensing mechanism

When operated at high temperature, tungsten oxide sensors are known to behave as n-type semiconductors. One of the conceivable mechanisms for the p-type conductive behavior at RT is the formation of an inversion layer on the surface of WO_3 nanorods. Owing to the fact that bulk defects equilibrate quite slowly at RT, surface conduction is dominant. The surface of the semiconductor is composed of a surface layer and space charge layer. Because of the existence of large density of surface states which mainly was induced by dangling, structural defects and gas adsorption, too many charges accumulated on the surface layer, which led to an aggregation layer, depletion layer, or even inversion space-charge layer below the surface layer of the semiconductor as shown in Fig. 8. In the energy-level diagram of the n-type semiconductor, the Fermi level approaches the bottom of the conduction band and above the intrinsic level, as shown in Fig. 8(a).

When the WO_3 nanorods sensors are exposed to air, oxygen molecules are absorbed on the surface of WO_3 nanorods and form chemisorbed oxygen species by capturing electrons from the conduction band of WO_3 nanorods (Eqs. (1) and (2)). Then the energy level of WO_3 nanorods is upswept and the depletion layer is formed, as shown in Fig. 8(b). When the WO_3 nanorods sensors are exposed to NO_2, as a powerful oxidizing gas with strong electron-withdrawing power, NO_2 is capable of competitively capturing electrons not only from the conduction band of WO_3 nanorods but also from chemisorbed oxygen species (Eqs. (3)–(5)). Besides the high surface areas that make the surface more actively adsorb O_2 or NO_2, there exists a non-stoichiometry monoclinic W_3O which has a large amount of oxygen vacancies. It easily adsorbs O_2 or NO_2 to stabilization.[30] Then with the continuous accumulation of negative charges, too many negative charges aggregate in the surface layer and the inversion layer in which holes become the main charge carrier is gradually generated, as shown in Fig. 8(c). In the energy-level diagram, the Fermi level appears below intrinsic level.

$$O_2(\text{gas}) \leftrightarrow O_2(\text{ads}), \tag{1}$$

$$O_2(\text{ads}) + e^- \leftrightarrow O_2^-(\text{ads}), \tag{2}$$

$$NO_2(\text{gas}) \leftrightarrow NO_2(\text{ads}), \tag{3}$$

$$NO_2(\text{ads}) + e^- \leftrightarrow NO_2^-(\text{ads}), \tag{4}$$

$$NO_2(\text{ads}) + O_2^- + 2e^- \leftrightarrow NO_2^-(\text{ads}) + 2O^-(\text{ads}). \tag{5}$$

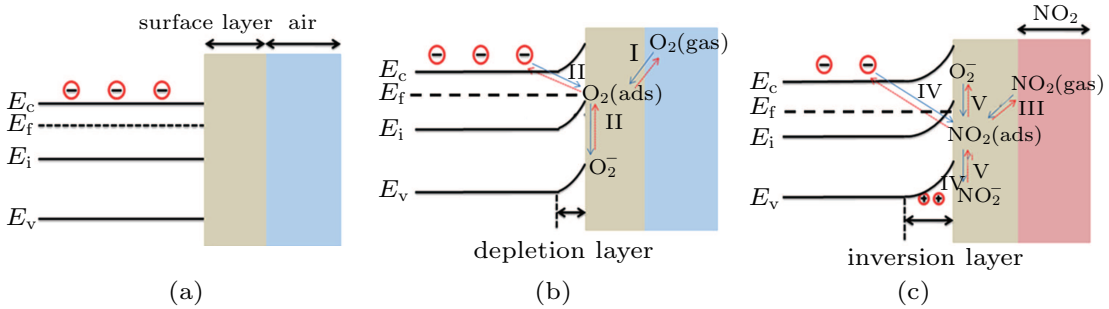


Fig. 8. (color online) Schematic energy-level diagram of (a) n-type semiconductor, (b) the formation of depletion layer, (c) the formation of inversion layer.

3.4. Repeatability

For practical use, the repeatability of the gas sensors is also an important quality factor. Reversible and reproducible responses of the 400-°C-annealed gas sensor upon periodic exposure to NO_2 gas of 1 ppm are presented in Fig. 9 with five switching on/off cycles. Notably, the sensor shows a similar response value and response–recovery time, which suggest an excellent repeatability and stability. It is well known that the high crystallinity of the WO_3 nanorods is responsible for the high stability of the sensor.[31]

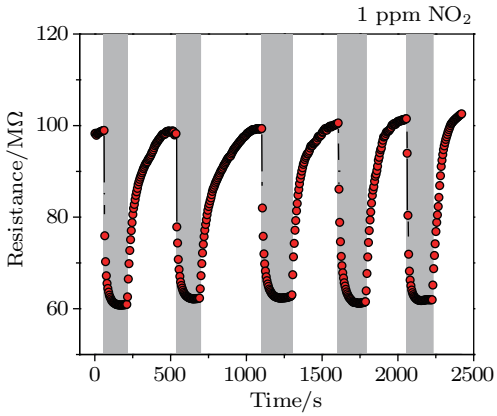


Fig. 9. (color online) Electrical resistance changes of the sensor based on 400-°C annealed WO_3 nanorods as a function of time for five cycles at room temperature with 1 ppm of NO_2.

4. Conclusions

In summary, WO_3 nanorods were successfully synthesized through the hydrothermal method. The microstructures and crystalline phases of both pristine and annealed WO_3 nanorods were investigated by SEM, EDS, HRTEM, and XRD. The test results showed that a fracture occurred during annealing treatment. The 300-°C- and 400-°C-annealed samples became shorter than the original WO_3 nanorods but the 500-°C-annealed nanorods were shaped into nanoparticles. At the same time the XRD patterns indicated that a new crystalline phase W_3O came into being during the thermal treatment process. Moreover, the appearance of a low oxidized tungsten phase W_3O was beneficial to the enhancement of the gas sensing performance of WO_3 nanorods. Response measurements of annealed samples performed at RT showed that all the annealed WO_3 nanorods sensors presented p-type behaviors. We suppose the transition mechanism from n to p-type to be that an inversion layer formed in the space charge layer when the sensors were exposed to NO_2 at room temperature. Compared with the 300-°C- and 500-°C-annealed samples, the 400-°C-annealed sample has higher response, quicker response/recovery speed, and more stable repeatability. The excellent gas sensing properties can be attributed to its moderate crystallinity, larger specific surface areas and more oxygen vacancy. This result is important for the future research and development of a gas sensor based on hexagonal WO_3 nanorods, which favors low power consumption, high sensitivity and integration technology.

References

[1] Afzal A, Cioffi N, Sabbatini L and Torsi L 2012 *Sens. Actuators B* **171** 25
[2] Heidari E K, Zamani C, Marzbanrad E, Raissi B and Nazarpour S 2010 *Sens. Actuators B* **146** 165
[3] Lee Y L, Tsai W C, Chang C H and Yang Y M 2001 *Appl. Surf. Sci.* **172** 191
[4] Lee J H, Kim J, Seo H W, Song J W, Lee E S, Won M and Han C S 2008 *Sens. Actuators B* **129** 628
[5] Kim B G, Lim D G, Park J H, Choi Y J and Park J G 2011 *Appl. Surf. Sci.* **257** 4715
[6] Karthigeyan A, Gupta R P, Scharnagl K, Burgmair M, Zimmer M, Sharma S K and Eisele I 2001 *Sens. Actuators B* **78** 69
[7] Kunimoto A, Abe N, Uchida H and Katsube T 2000 *Sens. Actuators B* **65** 122
[8] Tamaki J, Hashishin T, Uno Y, Dao D V and Sugiyama S 2008 *Sens. Actuators B* **132** 234
[9] Kim Y S 2009 *Sens. Actuators B* **137** 297
[10] Bai S, Zhang K, Luo R, Li D, Chen A and Liu C C 2012 *J. Mater. Chem.* **22** 12643
[11] Kim S J, Hwang I S, Choi J K and Lee J H 2011 *Thin Solid Films* **519** 2020
[12] Zhang C, Debliquy M, Boudiba A, Liao H and Coddet C 2010 *Sens. Actuators B* **144** 280
[13] Meng D, Yamazaki T, Shen Y, Liu Z and Kikut T 2009 *Appl. Surf. Sci.* **256** 1050
[14] Sun S, Chang X and Li Z 2010 *Mater. Res. Bull.* **45** 1075
[15] Malag'u C, Guidi V, Carotta M C and Martinelli G 2004 *Appl. Phys. Lett.* **84** 4158
[16] Malag'u C, Carotta M C, Gherardi S, Guidi V, Vendemiati B and Martinelli G 2005 *Sens. Actuators B* **108** 70
[17] Qin Y, Shen W, Li X and Hu M 2011 *Sens. Actuators B* **155** 646
[18] Liu Z F, Yamazaki T, Shen Y B, Kikuta T and Nakatani N 2007 *Sens. Actuators B* **128** 173
[19] Moseley P T 1997 *Meas. Sci. Technol.* **8** 223
[20] Williams D E 1999 *Sens. Actuators B* **57** 1
[21] Ahmad M Z, Sadek A Z, Ou J Z, Yaacob M H, Latham K and Wlodarski W 2013 *Mater. Chem. Phys.* **141** 912
[22] Chen D, Yin L, Ge L, Fan B, Zhang R, Sun J and Sha G 2013 *Sens. Actuators B* **185** 445
[23] Ahmad M Z, Wisitsoraat A, Zoolfakar A S, Kadir R A and Wlodarski W 2013 *Sens. Actuators B* **183** 364
[24] Liu Z, Miyauchi M, Yamazaki T and Shen Y 2009 *Sens. Actuators B* **140** 514
[25] You L, Sun Y F, Ma J, Guan Y, Sun J M, Du Y and Lu G Y 2011 *Sens. Actuators B* **157** 401
[26] Qin Y, Hu M and Zhang J 2010 *Sens. Actuators B* **150** 339
[27] Li Y H, Zhao Y M, Ma R Z, Zhu Y Q, Fisher N, Jin Y Z and Zhang X P 2006 *J. Phys. Chem. B* **110** 18191
[28] Pfeifer J, Badaljan E, TekulaBuxbaum P, Kovacs T, Geszti O and Toth A L 1996 *J. Cryst. Growth* **169** 727
[29] Wu Y, Hu M and Wei X 2014 *Chin. Phys. B* **23** 040704
[30] Cacucci A, Potin V, Imhoff L, Marco de Lucas M C and Martin N 2012 *Thin Solid Films* **520** 4778
[31] Tong P V, Hoa N D, Quang V V, Duy N V and Hieu N V 2013 *Sens. Actuators B* **183** 372